Mobilization of lithospheric mantle carbon during the Palaeocene-Eocene thermal maximum

Thomas Gernon (Thomas.Gernon@noc.soton.ac.uk)
University of Southampton https://orcid.org/0000-0002-7717-2092

Ryan Barr
University of Southampton

John Fitton
University of Edinburgh

Thea Hincks
University of Bristol

Jack Longman
Carl von Ossietzky University Oldenburg https://orcid.org/0000-0002-2725-2617

Andrew Merdith
Claude Bernard University Lyon 1

Ross Mitchell
Institute of Geology and Geophysics, Chinese Academy of Sciences https://orcid.org/0000-0002-5349-7909

Martin Palmer
University of Southampton

Article

Keywords: global warming, environmental change, lithospheric mantle carbon

Posted Date: March 22nd, 2021

DOI: https://doi.org/10.21203/rs.3.rs-333061/v1

Mobilization of lithospheric mantle carbon during the Palaeocene-Eocene thermal maximum

Thomas M. Gernon[a,*], Ryan Barr[a], J. Godfrey Fitton[b], Thea K. Hincks[a], Jack Longman[a,c], Andrew S. Merdith[d], Ross N. Mitchell[e], Martin R. Palmer[a]

[a]*School of Ocean & Earth Science, University of Southampton, Southampton SO14 3ZH, UK*
[b]*School of GeoSciences, University of Edinburgh, James Hutton Road, Edinburgh EH9 3FE, UK*
[c]*Institute for Chemistry & Biology of the Marine Environment, University of Oldenburg, D-26129 Oldenburg, Germany*
[d]*Laboratoire de Géologie, Université of Lyon 1, France*
[e]*State Key Laboratory of Lithospheric Evolution, Institute of Geology & Geophysics, Chinese Academy of Sciences, Beijing 100029, China*

Abstract

The early Cenozoic exhibited profound environmental change influenced by plume magmatism, continental breakup, and opening of the North Atlantic Ocean. Global warming culminated in the transient (170 thousand year, kyr) hyperthermal event, the Palaeocene-Eocene thermal maximum (PETM) 56 million years ago (Ma). Although sedimentary methane release has been proposed as a trigger, recent studies have implicated carbon dioxide (CO_2) emissions from the coeval North Atlantic igneous province (NAIP). However, we calculate that volcanic outgassing from mid-ocean ridges and large igneous provinces associated with the NAIP yields only one-fifth of the carbon required to trigger the PETM. Rather, we show that volcanic sequences spanning the rift-to-drift phase of the NAIP exhibit a sudden and ~220-kyr-long intensification of volcanism coincident with the PETM, and driven by substantial melting of the sub-continental lithospheric mantle (SCLM). Critically, the SCLM is enriched in metasomatic carbonates and is a major carbon reservoir. We propose that the coincidence of the Iceland plume and emerging asthenospheric upwelling disrupted the SCLM and caused massive mobilization of this deep carbon. Our melting models and coupled tectonic–geochemical simulations indicate the release of >10^4 gigatons of carbon, which is sufficient to drive PETM warming. Our model is consistent with anomalous CO_2 fluxes during continental breakup, while also reconciling the deficit of deep carbon required to explain the PETM.

During the early Cenozoic, a major episode of continental breakup in the North Atlantic region (Fig. 1a) resulted in widespread magmatism and the opening of the North Atlantic Ocean[1,3]. Initially the Iceland plume caused regional uplift and a phase of subaerial volcanism lasting ~5 million years (Myr)[2,9,10]. Then, at ~56 million years ago (Ma), an incipient mid-ocean ridge developed[1] (Fig. 1d), coinciding with an order-of-magnitude increase in melt production rates[3], and accelerated westward migration of Greenland via ridge push[8] (Fig. 1e). This transitional phase of volcanism in the North Atlantic igneous province (NAIP) involved peak eruption rates of ~2.4 km^3 yr^{-1} (ref.[9]) and occurred contemporaneously with intense early Eocene warming, including the PETM[11].

During the PETM, sea surface temperatures increased by ~5°C (ref.[12]), ocean acidification occurred[13,14] and there was an abrupt and short-lived (~170 thousand year, kyr)[11,15] negative δ^{13}C carbon isotope excursion (Fig. 1c). It is thought that the release of approximately 1–1.5 × 10^4 gigatons (Gt) of carbon into the ocean-atmosphere system is necessary to account for these changes[14,16]. This massive carbon flux has been attributed to methane release associated with clathrate destabilization along continental shelves[17] and/or hydrothermal venting during interaction of magmas and organic-rich mudrocks[18]. However, on the basis of paired δ^{11}B–δ^{13}C data and carbon-cycle modeling[14], and B/Ca in planktic foraminifera[16], it has been proposed that triggering of the PETM required a short, sharp injection of a ^{13}C depleted source of carbon, possibly tied to volcanic outgassing across the NAIP.

To test this hypothesis, we estimated the combined CO_2 emissions from incipient mid-ocean ridge volcanism and large igneous provinces (LIPs) in the NAIP, parameterized by plate-tectonic reconstructions (Fig. 1b,d) and existing estimates of magmatic productivity[9] (Methods). In our model, we considered pre-eruptive CO_2 concentrations of 2 wt%, which are typical of flood basalt eruptions[19]. The associated CO_2 release from the ocean crust is then calculated from the ratio between the observed levels of magmatic production along the present-day mid-ocean ridge system (~18 km^3 yr^{-1}), and estimated CO_2 degassing fluxes along the modern global ridge system (7 × 10^{11} mol yr^{-1})[20]. This calculation suggests that ~10% of the CO_2 in the juvenile ocean crust is degassed at ridges. Using this estimate, the NAIP ridges likely produced ~1.1 × 10^3 Gt C during the PETM. This is an order of magnitude lower than the requisite ~1–1.5 × 10^4 Gt C (refs.[14,16]). Inclusion of the effects of LIP magmatism—assuming most probable eruption rates[9] and total degassing—yields less than one-fifth of the carbon needed to drive and sustain the PETM[14,16]. Furthermore, seafloor isochrons indicate that magmatic productivity along

*Corresponding author: Thomas.Gernon@noc.soton.ac.uk

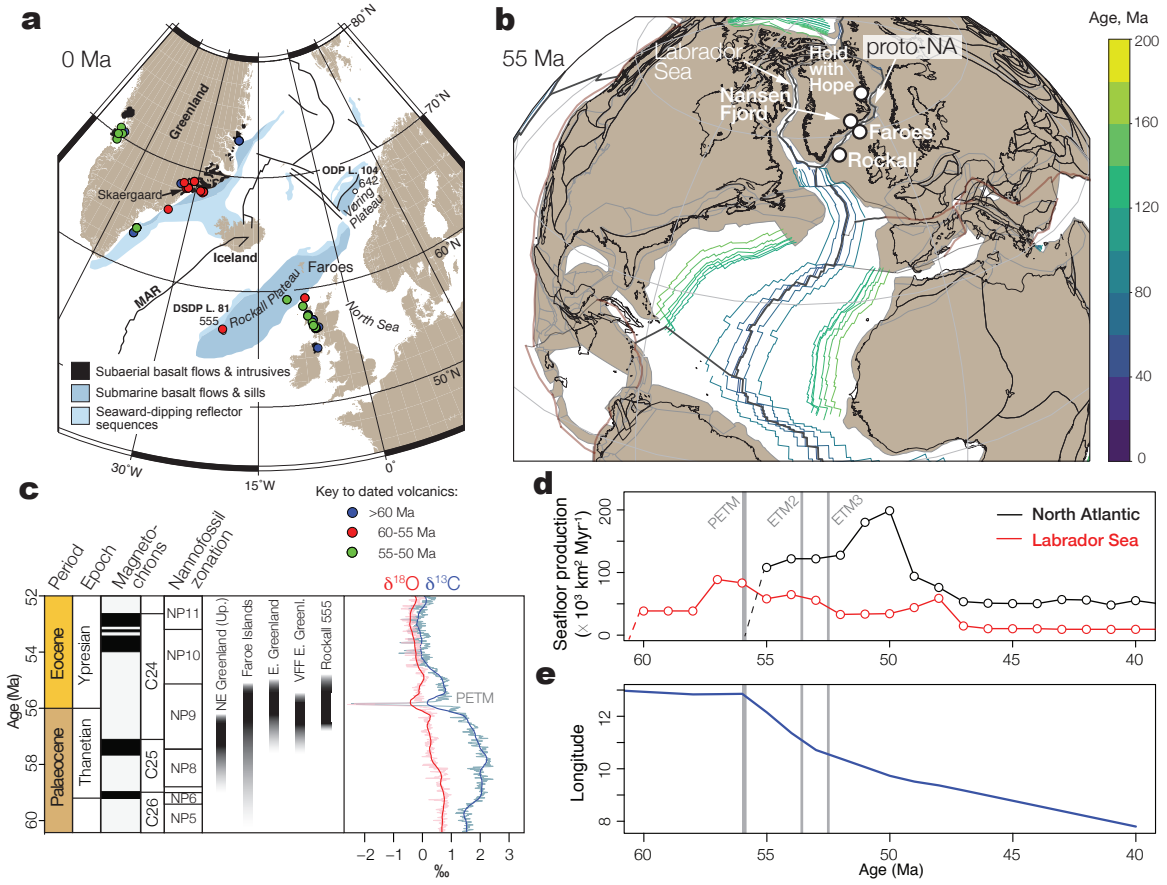

Figure 1. Early Cenozoic tectonic and magmatic evolution of the North Atlantic region | a, Map of the present-day North Atlantic region showing the distribution of Palaeocene–Eocene lava flows and intrusives [1], with dated volcanics denoted by colored symbols [2]. **b,** Plate tectonic reconstruction showing nascent ridge systems developing along the Labrador Sea and North Atlantic. **c,** Ages of the volcanic sections discussed (Up=Upper; VFF=Vandfaldsdalen Fm), defined by radiometric dates [1,3], magnetostratigraphy and nannofossil zonation [4,5,6], and corresponding carbon and oxygen isotope records showing the PETM isotope excursions (solid and faint lines show 1 Myr and 20 kyr locally weighted functions, respectively) [7]. **d,** Seafloor production rates for the Labrador Sea and North Atlantic, derived from GPlates (Methods), shown alongside the timing of Eocene hyperthermals. (**E**) Palaeolongitude of Greenland [8] indicating the onset of ocean crustal production in the North Atlantic and ridge push at 56 Ma.

the North Atlantic ridge peaked after, not during, early Eocene hyperthermals (Fig. 1d). Therefore, some other major, but transient, source of volcanic carbon appears to be required if the volcanic outgassing hypothesis [14,16] is correct.

We have investigated several volcanic sequences spanning the Palaeocene-Eocene boundary (Fig. 1c). The Deep Sea Drilling Project Leg 81 Site 555 lies on the Rockall Plateau (Fig. 1a), near the proto-North Atlantic ridge (Fig. 1b). Here, Phase 1 volcanism [21] (Fig. 2a) is coeval with the Milne Land basalts in East Greenland and the Middle to Upper Series lavas in the Faroe Islands [1] (Fig. 2b-c). In the Rockall sequence, we found a sharp increase in the frequency of volcanic tuffs just below the Palaeocene–Eocene boundary (Fig. 2a) (Methods). The PETM is defined by δ^{13}C, however the volcanostratigraphy in our study area is not conducive to developing a high-resolution carbon isotope stratigraphy (Methods). Therefore, we rely on a combination of radiometric, magnetostratigraphic and paleontological age constraints, in addition to well-defined sediment accumulation rate estimates (Methods). Mudstones interbedded with the uppermost tuffs contain the dinoflagellate cyst, *Apectodinium augustum* [27], which is biostratigraphically diagnostic of the PETM as it signifies a sudden prevalence of tropical sea-surface temperatures [28]. Based on sedimentation rates (50 cm ka^{-1}) [4], this volcanic flare-up lasted for 171–213 kyr, similar to the duration of the coeval PETM [11,15], and was followed by a sharp decline in volcanism [21]. The tuffs exhibit wide compositional diversity from basanites to dacites (Supplementary Figs. 1, 2a–b), an increased range of magnesium number (Mg#; to a maximum observed value of 63), and a marked shift to highly negative ϵNd signatures at ca. 56.03 Ma (Fig. 2a). This activity signals a step change in magmatic processes and volcanic unrest along the ridge, as recorded across a major area of the NAIP (>130,000 km^2) [1,29]. Sampled PETM-age tuffs are enriched in Rb and Ba and depleted in Nb and Sr (Supplementary Fig. 2c), and have similar compositions to some of the lowermost ('negative ash series') tuffs of the Danish Basin, which likely derive from nearby volcanoes along the continental shelf [29]. The geochemical similarities between tuffs from Rockall and the Danish Basin is consistent with paleogeography (Fig. 1b), palynological constraints [27] and the stratigraphic position of these tuffs towards the end of the PETM elsewhere in the NAIP [6].

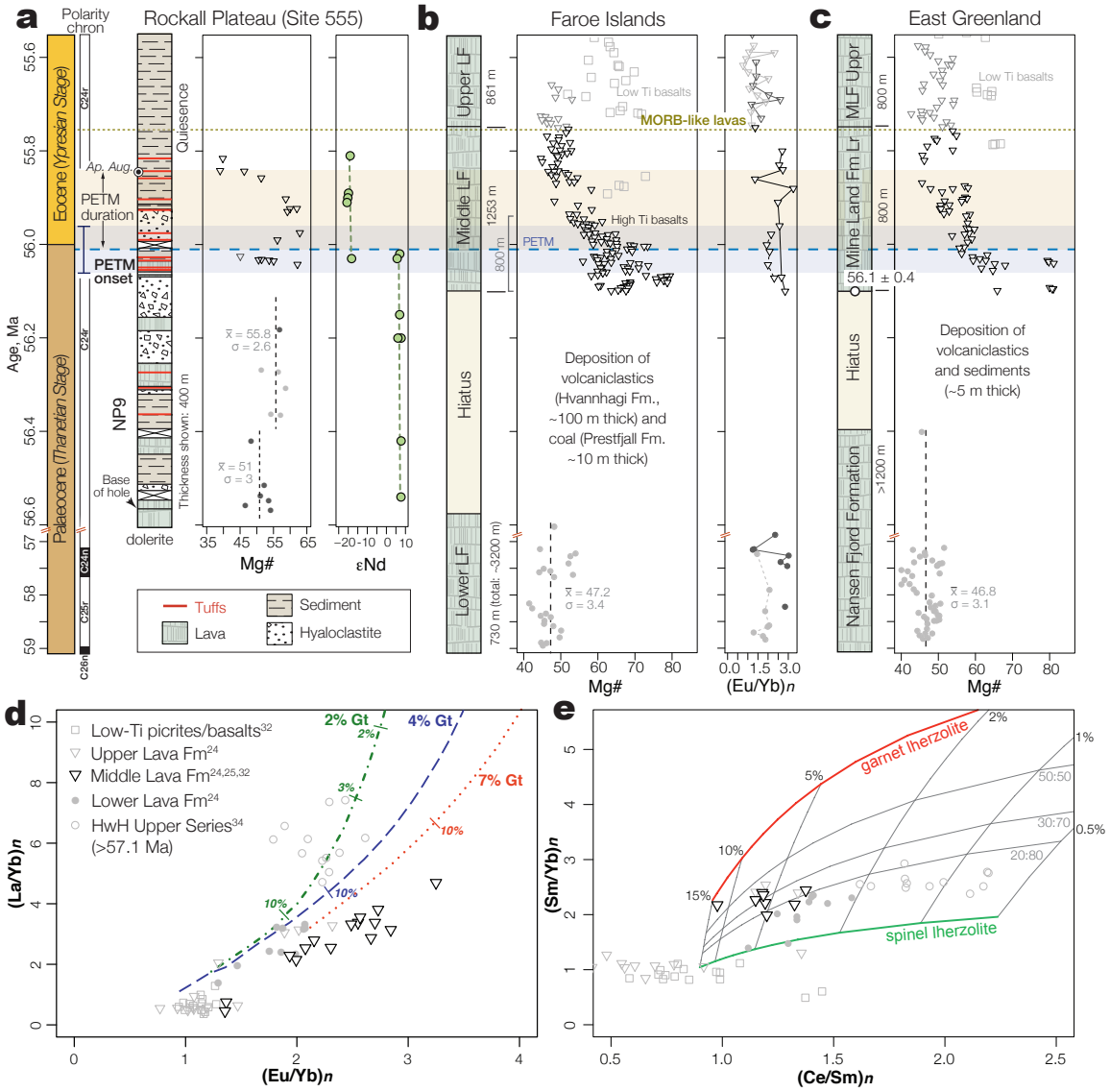

Fig. 2. Palaeocene-Eocene volcanostratigraphy and geochemistry of the proto-North Atlantic ridge. a, Simplified log of the Rockall 'Phase 1' sequence[21] showing lithologies, Mg# (i.e., 100 × molecular MgO/(MgO + FeO), where FeO is assumed to be 0.9FeOT), and ϵNd (Supplementary Fig. 1). **b,** Simplified log of the Faroes Basalt Formations[22], with Mg# and (Eu/Yb)*n* (chondrite-normalized[23]); Mg# data are from[22] and (Eu/Yb)*n* are from[24,25]; note the sharp transition to high Mg# (and enriched REE contents) at ca. 56.1 Ma[1], which is also observed in **c,** east Greenland (Milne Land Formation)[22]. **d,** (La/Yb)*n* vs (Eu/Yb)*n* of the Faroes and Hold with Hope (HwH) lavas (chondrite-normalized[23]) and modeled non-modal batch melting of a lherzolitic mantle source, adopted from[26], showing different degrees of melting of a garnet lherzolite (green, blue and red curves). **e,** (Sm/Yb)*n* vs (Ce/Sm)*n* and an REE melting model (Methods), showing percentage melt along the top and the relative proportions of garnet- and spinel-lherzolites from 100% gt-lherzolite (red curve) to 100% sp-lherzolite (green curve). Both models indicate that the Faroes Middle Lava Formation (i.e., high Mg# basalts in the lower 500 m of the MLF; see (**b**), that erupted immediately prior to and during the PETM, experienced the highest degrees of melting of a mantle source containing $\gtrsim$10% garnet.

Interpretation of geochemical data from the Rockall tuffs is complicated because they derive from diverse sources and have experienced varying degrees of seafloor weathering[21]. Hence, we next studied the coeval thick basaltic lava sequences that were emplaced subaerially near the ridge axis (Fig. 1). The Palaeocene-Eocene lavas of the Faroe Islands and East Greenland (Fig. 1b) are ideally suited because, unlike the contemporaneous lavas in SE Greenland[30], they are minimally affected by crustal contamination[22,24,31]. The base of the Milne Land Formation in East Greenland, which correlates with the base of the Middle Lava Series of the Faroes[1,22] (Fig. 2b-c; hereafter both referred to as 'MLF'), is dated at 56.1 ± 0.4 Ma and the duration of activity is well constrained[1,3] (Fig. 2). Thus, the base of the MLF correlates with (or shortly predates) the intensification of volcanism at Rockall Plateau (Fig. 2a).

We estimate that the 1.25 km-thick MLF package[1,22] was emplaced over 200–300 kyr, yielding an average eruption rate of ~4–6 m kyr^{-1}, but potentially an order of magnitude higher early in the eruptive cycle[1]. At the base of the sequence, thick (>100 m) pyroclastic deposits, also reported in Greenland[22], signal an early volatile-rich explosive phase. The overlying tholeiitic lavas are characterized by a sharp increase in Mg#, from values of ~52 throughout the Lower Lava Formation[22] to >80 in the basal MLF (Fig. 2b-c). The basal lavas are coincident (within dating uncertainties) with the onset of the PETM[11]. Many of these lavas are highly magnesian[32] (e.g., with MgO = 24%), implying hot liquidus temperatures, and are locally characterized by massive olivine accumulation[22]. They also exhibit high TiO_2 contents (typically 1.5–2.5 wt.%), and enrichment in Light Rare Earth Elements (LREEs), e.g., $(La/Yb)_n$ = 2–3, and $(Eu/Yb)_n$ >2.5 (Fig. 2b)[24,25]. This unusual pulse of high-Ti magmatism, similar to that of the Jurassic Karoo flood basalts in southern Africa[26], generated the long-lived (~300 kyr)[1] Skaergaard layered igneous intrusion at 55.75 ± 0.35 Ma (Fig. 1a)[1]. Finally, the Upper Lava Formation (Fig. 2b-c) signifies an abrupt shift to low-Ti depleted MORB-like basalts[22,24,25] (Fig. 2d-e), thus, there is evidence that the early (high Mg#) MLF volcanism was both transient[1] (~227 kyr) and chemically anomalous (Fig. 2).

The geochemical compositions of these lavas have been attributed to partial melting of the SCLM during asthenospheric upwelling[24], a model that is supported by studies of their feeder intrusions[31,32]. To test this hypothesis further, we applied two models of mantle melting. First, we adopted a non-modal batch melting model of a garnet-bearing lherzolitic mantle source[26] (Fig. 2d). For the second model, we estimated melt percentage based on average lherzolite mineralogy, average partition coefficients, and a plume composition based on primitive basalt (Fig. 2e) (Methods). Both models suggest that the MLF experienced a high degree of melting, up to ~13%, but typically in the range of 4–8%, with their high $(Sm/Yb)_n$ ratios (2–2.5) requiring ~20–>50% of garnet lherzolite in the mantle source (Fig. 2e). Metasomatism in the mantle source region has already been documented in this region at precisely this time[33] and invoked to explain the compositional characteristics of these high-Ti basalts, notably their LREE enrichment and variable Nb and Ta anomalies[31,32]. The composition of the MLF is compatible with enhanced melting of metasomatized SCLM by the Iceland plume, just prior to full seafloor spreading at c. 55.8 Ma[25] (Figs. 2b–c).

The trace element compositions show that the degree of melting varies systematically through the Faroes sequence (Fig. 2e), with the Lower Lava Formation (Fig. 2b-c) representing a relatively low degree of melting (2–5%; Fig. 2e). To expand the dataset, lavas from farther along the ridge axis in northeast Greenland are included (Hold with Hope)[34] (Fig. 1b), which have an upper age of ca. 57 Ma (C25n–C24r)[10]. These lavas exhibit geochemical characteristics that have been attributed to the incorporation of SCLM during melting[10,34]. Our model confirms a low degree of melting (0.5–2%) of a variably garnet-rich lherzolite source (Fig. 2e). Taken together, these observations confirm an up-section increase in the involvement of SCLM in melting during the late Palaeocene, peaking at the PETM (Fig. 2e), then rapidly declining in intensity prior to full continental breakup. There is possible evidence for this peak in Palaeocene–Eocene[5] basaltic lavas of the Vandfaldsdalen Formation in central east Greenland[35]. These lavas exhibit Nd, Sr and Pb isotope signatures indicative of an SCLM component[35]. Assimilation of the deep SCLM is particularly important because this zone is metasomatically enriched in carbonates, and is thus a major carbon reservoir[36,37,38].

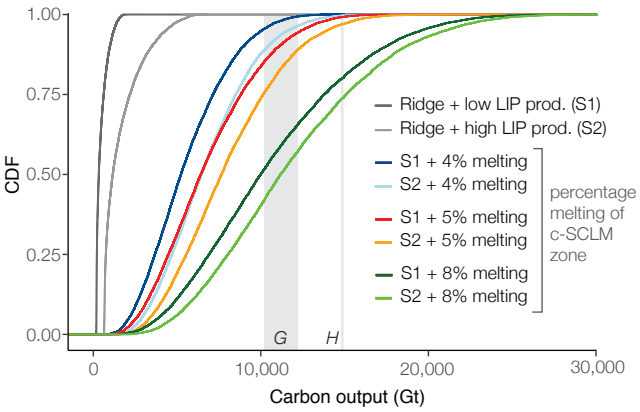

Figure 3. Simulations of volcanic carbon release during the PETM. Results are plotted as cumulative distribution functions (CDFs). The gray lines show the estimated carbon output from ridge volcanism and LIPs alone; with S1 and S2 showing low (0.6 km^3 yr^{-1}) and high (2.4 km^3 yr^{-1}) LIP eruption rate scenarios[9], respectively (Supplementary Fig. 3) (see Methods). The coloured lines show the effects of adding 4% to 8% carbonated (c–) SCLM melt along the incipient ridge during breakup. The gray vertical bars denote the carbon output necessary to drive and sustain PETM warming estimated by Gutjahr et al.[14] (labelled *G*; 10,200–12,200 Gt C), and Haynes & Hönisch[16] (labelled *H*; 14,900 Gt C).

The process of ocean basin formation significantly disrupts the >100 km thick SCLM[39]. Because carbonates are only stable in the mantle at high pressures[37] (~3 GPa at 1300°C)[39], significant carbon release will only occur when extending cratons are at least 130 km thick[39]. Seismic tomography indicates that the lithosphere in central Greenland (i.e., the locus of the Iceland plume at 56 Ma[2]) is 180 km thick[40]; firmly meeting this criterion. Xenoliths provide additional evidence for coeval volatile-rich metasomatism in the deep SCLM be-

neath Greenland, as does the occurrence of carbonatite magmatism across the wider NAIP at this time[33]. Therefore, breakup of the North Atlantic craton provided a perfect combination of conditions: the availability of sufficiently thick metasomatized SCLM, analogous to the present-day Tanzanian craton in the East African Rift System[36]; the long-term thermo-mechanical weakening and erosion of the SCLM by the Iceland plume[2], broadly analogous to that proposed for the Permo-Triassic Siberian Traps[38]; and the initiation of asthenospheric upwelling that induced vigorous interaction between anomalously hot melt and the weakened SCLM[37,39]. A key aspect of our hypothesis is that the most extensive period of volcanic CO_2 outgassing (~50 Mt C yr^{-1}) occurred over a short period (~171–227 kyr), and likely peaked just prior to PETM onset (Fig. 2b-c). While continental rift volcanism is associated with enhanced CO_2 fluxes over millions of years, petrological and numerical models suggest that there is an initial short period of deep redox controlled carbonatitic to aillikitic melting (i.e., high CO_2) that is followed by more widespread metasomatism of the shallower asthenosphere and generation of less CO_2-rich melts through decompression melting[37,39].

Both the thickness and composition of the NAIP lithospheric mantle make it a viable source of large amounts of carbon from the deep, carbonated SCLM during the PETM. A fundamental aspect of our model is that the occurrence of continental rifting opens a wide area along the incipient ridge to SCLM influence. This contrasts with the end-Permian Siberian Traps, where there is no evidence for large-scale lithospheric stretching during eruption[38]. Indeed, it has been suggested that relics of this SCLM that delaminated during North Atlantic breakup can explain residual enriched 'EM1' components present in the Icelandic mantle today[41,42,43]. The question is then whether this process can contribute enough carbon to help explain the PETM carbon isotope excursion[14,16]. Recent estimates suggest that the SCLM may contain 5–8% CO_2, or possibly more[37]. The present-day East African Rift offers a lower bound. Here, lateral advection of SCLM along the craton margins results in an order of magnitude increase in the volcanic CO_2 flux compared to the background crustal contribution[36].

To more accurately quantify the potential influence of rift-related SCLM disturbance, we advance on the approach taken by Sobolev et al.[38] to estimate the most probable carbon release scenarios for the PETM. We performed 10,000 Monte Carlo calculations using CO_2 contents ranging from 1–8%, and length-scales of the carbonated SCLM in the narrow melting zone below the nascent ridge crest[39] based on tectonic reconstructions, chemical tomography and lithospheric models (tables S7–S8) (see Methods). These calculations suggest that only 4–8% of this zone needs to melt to exceed the requisite $>10^4$ Gt C for PETM warming[14,16] (Fig. 3). This is consistent with the modeled 5–8% melting of a garnet-rich lherzolite during the PETM (Fig. 2d-e), and earlier estimates that the intrusive feeders of these Ti-rich basalts formed by 4%[32] to 7%[31] batch melting of fertile, metasomatized lherzolites in the SCLM[31].

The step change in NAIP magmatic productivity[3] immediately prior to the PETM gave rise to widespread volcanic unrest (Figs. 2, 4). While some volcanic tuffs at Rockall Plateau are likely linked to the MLF (especially those with high Mg#), many of these tuffs are likely genetically unrelated, but are rather a manifestation of the general increase in mantle melting, and fluxes of magma and volatiles through volcanic centres along the continental shelf at this time[29]. The Rockall sequence places firm constraints on both the timing and duration of this climate-altering phase of volcanism at ~171–213 kyr, which is similar to the duration of the lower, high Mg#, part of the MLF (Fig. 2). This surge in regional volcanism could explain the wide variability in the composition of tuffs belonging to the Danish negative ash series[29]. Indeed, the chemical weathering of extensive tephra blankets may also explain the large decrease in $^{187}Os/^{188}Os$ observed just prior to PETM onset at Svalbard[44].

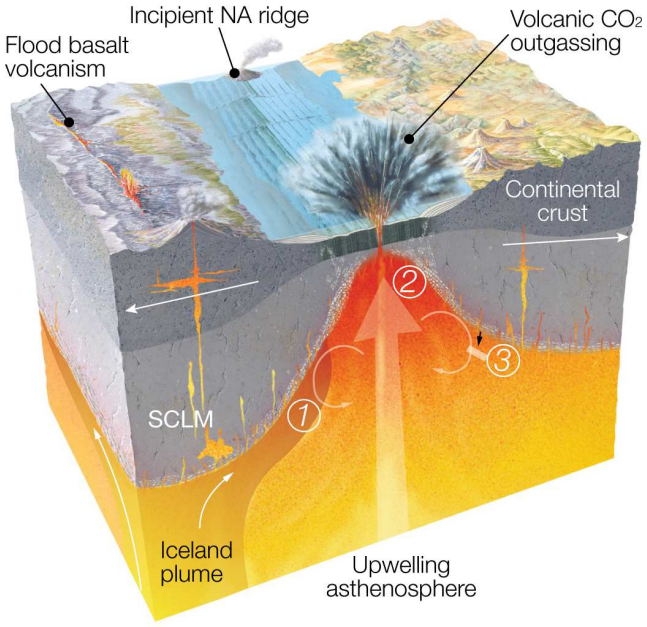

Figure 4. Volcanic carbon release in the North Atlantic during the PETM. Model stages: **1,** progressive thermo-mechanical weakening of the sub-continental lithospheric mantle (SCLM) by the Iceland plume; **2,** disruption of the ruptured metasomatized SCLM zone by incipient asthenospheric upwelling; **3,** delamination of carbonated fragments of the deep SCLM during lithospheric stretching, which generate the enduring enriched components ('EM1') still present in the Icelandic mantle today[41].

Enhanced melting of the SCLM during continental breakup resulted from an unusual combination of conditions in the NAIP (Fig. 4) and provides a direct mechanism to dramatically increase the outgassing of deep carbon. We have shown that this process reached peak intensity just prior to, and during, the PETM (Fig. 2), satisfying the requirement for a massive surge of ^{13}C depleted carbon[14,16] (Fig. 3). The melting of SCLM can result in a fivefold increase in volcanic CO_2 output, reconciling an apparent major deficit of carbon from 'background' ridge and LIP volcanism (see curves S1–S2 on Fig. 3). The mobilization of carbon from the SCLM is consistent with the inferred disruption of the metasomatized lithosphere during breakup of the North Atlantic craton[41], and the anomalously high CO_2 fluxes from SCLM along craton margins during extension[36,39].

Our data-driven models of the PETM demonstrably support the proposal that large-scale lithospheric melting can induce global warming[38], if the tectonic setting is primed to facilitate intensive volcanic CO_2 degassing (Fig. 4). Our study highlights the critical role that solid Earth degassing plays in driving abrupt shifts in climate, and in promoting fundamental reorganisation of Earth's surface environment and biosphere.

Online content

Any methods, additional references, Nature Research reporting summaries, source data, extended data, supplementary information, acknowledgements, peer review information; details of author contributions and competing interests; and statements of data and code availability are available at https://doi.org/10.1038/s12345-111-2222-3.

References

1. M. Storey, R.A. Duncan, and C.C. Swisher. Paleocene-Eocene Thermal Maximum and the opening of the Northeast Atlantic. *Science*, 316:587–589, 2007.
2. B. Steinberger, E. Bredow, S. Lebedev, A. Schaeffer, and Trond H. T. Widespread volcanism in the Greenland–North Atlantic region explained by the Iceland plume. *Nature Geoscience*, 12(1):61–68, 2019.
3. M. Storey, R. A. Duncan, and C. Tegner. Timing and duration of volcanism in the North Atlantic Igneous Province: Implications for geodynamics and links to the iceland hotspot. *Chemical Geology*, 241:264–281, 2007.
4. J. Backman, A. C. Morton, D. G. Roberts, S. Brown, K. Krumsiek, and R. M. Macintyre. Geochronology of the Lower Eocene and Upper Paleocene sequences of Leg 81 - Deep Sea Drilling Project (Rockall Plateau). In *DSDP Initial Reports*, volume 81, chapter 38, pages 877–882. 1984.
5. H. Nøhr-Hansen. Palynostratigraphy of the Cretaceous–lower Palaeogene sedimentary succession in the Kangerlussuaq Basin, southern East Greenland. *Review of Palaeobotany and Palynology*, 178:59–90, 2012.
6. E. W. Stokke, M. T. Jones, J. E. Tierney, H. H. Svensen, and J. H. Whiteside. Temperature changes across the Paleocene-Eocene Thermal Maximum – a new high-resolution TEX_{86} temperature record from the Eastern North Sea Basin. *Earth and Planetary Science Letters*, 544:116388, 2020.
7. T. Westerhold, N. Marwan, A. J. Drury, D. Liebrand, C. Agnini, E. Anagnostou, J. S. K. Barnet, S. M. Bohaty, D. De Vleeschouwer, F. Florindo, T. Frederichs, D. A. Hodell, A. E. Holbourn, D. Kroon, V. Lauretano, K. Littler, L. J. Lourens, M. Lyle, H. Pälike, U. Röhl, J. Tian, R. H. Wilkens, P. A. Wilson, and J. C. Zachos. An astronomically dated record of Earth's climate and its predictability over the last 66 million years. *Science*, 369(6509):1383–1387, 2020.
8. R. N. Mitchell, T. M. Kilian, and D. A. D. Evans. Supercontinent cycles and the calculation of absolute palaeolongitude in deep time. *Nature*, 482(7384):208–211, 2012.
9. O. Eldholm and K. Grue. North Atlantic volcanic margins: Dimensions and production rates. *Journal of Geophysical Research*, 99(B2):2955–2968, 1994.
10. A. D. Saunders, J. G. Fitton, A. C. Kerr, M. J. Norry, and R. W. Kent. The north atlantic igneous province. In J. J. Mahoney and M. F. Coffin, editors, *Large Igneous Provinces*, volume 100, pages 45–94. AGU Geophysical Monograph Series, 1997.
11. R. E. Zeebe and L. J. Lourens. Solar System chaos and the Paleocene–Eocene boundary age constrained by geology and astronomy. *Science*, 365(6456):926–929, 2019.
12. Joost Frieling, Holger Gebhardt, Matthew Huber, Olabisi A. Adekeye, Samuel O. Akande, Gert-Jan Reichart, Jack J. Middelburg, Stefan Schouten, and Appy Sluijs. Extreme warmth and heat-stressed plankton in the tropics during the Paleocene-Eocene Thermal Maximum. *Science Advances*, 3(3):e1600891, 2017.
13. J. C. Zachos, G. R. Dickens, and R. E. Zeebe. An early Cenozoic perspective on greenhouse warming and carbon-cycle dynamics. *Nature*, 451:279–283, 2008.
14. M. Gutjahr, A. Ridgwell, P. F. Sexton, E. Anagnostou, P. N. Pearson, H. Pälike, R. D. Norris, E. Thomas, and G. L. Foster. Very large release of mostly volcanic carbon during the Palaeocene–Eocene Thermal Maximum. *Nature*, 548(7669):573–577, 2017.
15. U. Röhl, T. Westerhold, T. J. Bralower, and J. C. Zachos. On the duration of the Paleocene-Eocene thermal maximum (PETM). *Geochemistry, Geophysics, Geosystems*, 8(12):Q12002, 2007.
16. L. L. Haynes and B. Hönisch. The seawater carbon inventory at the Paleocene–Eocene Thermal Maximum. *Proceedings of the National Academy of Sciences*, page 202003197, 2020.
17. G. R. Dickens, J. R. O'Neil, D. K. Rea, and R. M. Owen. Dissociation of oceanic methane hydrate as a cause of the carbon isotope excursion at the end of the Paleocene. *Paleoceanography*, 10(6):965–971, 1995.
18. H. Svensen, S. Planke, A Malthe-Sørenssen, B. Jamtveit, R. Myklebust, T. Rasmussen-Eldem, and S.S. Ray. Release of methane from a volcanic basin as a mechanism for initial Eocene global warming. *Nature*, 429:542–545, 2004.
19. S. Self, T. Thordarson, and M. Widdowson. Gas fluxes from flood basalt eruptions. *Elements*, 1(5):283–287, 2005.
20. D. Chavrit, E. Humler, and O. Grasset. Mapping modern CO_2 fluxes and mantle carbon content all along the mid-ocean ridge system. *Earth and Planetary Science Letters*, 387:229–239, 2014.
21. A. C. Morton and J. B. Keene. Paleogene pyroclastic volcanism in the southwest Rockall Plateau - Deep Sea Drilling Project Leg 81. In *DSDP Initial Reports*, volume 81, chapter 19, pages 633–643. 1984.
22. L. M. Larsen, R. Waagstein, A. K. Pedersen, and M. Storey. Trans-Atlantic correlation of the Palaeogene volcanic successions in the Faeroe Islands and East Greenland. *Journal of the Geological Society*, 156(6):1081–1095, 1999.
23. W. V. Boynton and P. Henderson. *Chapter 3 - Cosmochemistry of the Rare Earth Elements: Meteorite Studies*, volume 2, pages 63–114. Elsevier, 1984.
24. C. Gariépy, J. Ludden, and C. Brooks. Isotopic and trace element constraints on the genesis of the Faeroe lava pile. *Earth and Planetary Science Letters*, 63(2):257–272, 1983.
25. J-G. Schilling and A. Noe-Nygaard. Faeroe-Iceland plume: Rare-Earth evidence. *Earth and Planetary Science Letters*, 24(1):1–14, 1974.
26. F. Jourdan, H. Bertrand, U. Schärer, J. Blichert-Toft, G. Féraud, and A. B. Kampunzu. Major and trace element and Sr, Nd, Hf, and Pb isotope compositions of the Karoo Large Igneous Province, Botswana–Zimbabwe: Lithosphere vs mantle plume contribution. *Journal of Petrology*, 48(6):1043–1077, 2007.
27. S. Brown and C. Downie. Dinoflagellate cyct biostratigraphy of late Paleocene and early Eocene sediments from holes 552, 553A, and 555 - Deep Sea Drilling Project Leg 81 (Rockall Plateau). In *DSDP Initial Reports*, volume 81, chapter 13, pages 565–579. 1984.
28. A. Sluijs, S. Schouten, M. Pagani, M. Woltering, H. Brinkhuis, J. S. Sinninghe Damsté, G. R. Dickens, M. Huber, G. J. Reichart, R. Stein, J. Matthiessen, L. J. Lourens, N. Pedentchouk, J. Backman, K. Moran, and the Exhibition 302 Scientists. Subtropical Arctic Ocean temperature during the Palaeocene/Eocene thermal maximum. *Nature*, 441:610–613, 2006.
29. L. M. Larsen, J. G. Fitton, and A. K. Pedersen. Paleogene volcanic ash layers in the Danish Basin: compositions and source areas in the North Atlantic Igneous Province. *Lithos*, 71:47–80, 2003.
30. J. G. Fitton, L. M. Larsen, A. D. Saunders, B. S. Hardarson, and P. D. Kempton. Palaeogene continental to oceanic magmatism on the SE Greenland continental margin at 63 °N: a review of the results of Ocean Drilling Program Legs 152 and 163. *Journal of Petrology*, 41(7):951–966, 2000.
31. J. Hansen, J. Davidson, D. Jerram, C. Ottley, and M. Widdowson. Contrasting TiO_2 compositions in early Cenozoic mafic sills of the Faroe Islands: An example of basalt formation from distinct melting regimes. *Earth Sciences*, 8(5):235–267, 2019.
32. P. M. Holm, N. Hald, and R. Waagstein. Geochemical and Pb–Sr–Nd isotopic evidence for separate hot depleted and Iceland plume mantle sources for the Paleogene basalts of the Faroe Islands. *Chemical Geology*, 178(1):95–125, 2001.

33. S. Aulbach, J. Sun, S. Tappe, H. E Höfer, and A. Gerdes. Volatile-rich metasomatism in the cratonic mantle beneath SW Greenland: Link to kimberlites and mid-lithospheric discontinuities. *Journal of Petrology*, 58(12):2311–2338, 2018.
34. M. F. Thirlwall, B. G. J. Upton, and C. Jenkins. Interaction between Continental Lithosphere and the Iceland Plume—Sr-Nd-Pb Isotope Geochemistry of Tertiary Basalts, NE Greenland. *Journal of Petrology*, 35(3):839–879, 06 1994.
35. P. M. Holm. Nd, Sr and Pb isotope geochemistry of the Lower Lavas, E Greenland Tertiary Igneous Province. *Geological Society, London, Special Publications*, 39(1):181, 1988.
36. J. D. Muirhead, T. P. Fischer, S. J. Oliva, A. Laizer, J. van Wijk, C. A. Currie, H. Lee, E. J. Judd, E. Kazimoto, Y. Sano, N. Takahata, C. Tiberi, S. F. Foley, J. Dufek, M. C. Reiss, and C. J. Ebinger. Displaced cratonic mantle concentrates deep carbon during continental rifting. *Nature*, 582(7810):67–72, 2020.
37. S. F. Foley and T. P. Fischer. An essential role for continental rifts and lithosphere in the deep carbon cycle. *Nature Geoscience*, 10(12):897–902, 2017.
38. S. V. Sobolev, A. V. Sobolev, D. V. Kuzmin, N. A. Krivolutskaya, A. G. Petrunin, N. T. Arndt, V. A. Radko, and Y. R. Vasiliev. Linking mantle plumes, large igneous provinces and environmental catastrophes. *Nature*, 477(7364):312–316, 2011.
39. W. Gorczyk and C. M. Gonzalez. CO_2 degassing and melting of metasomatized mantle lithosphere during rifting–Numerical study. *Geoscience Frontiers*, 10(4):1409–1420, 2019.
40. F. A. Darbyshire, T. B. Larsen, K. Mosegaard, T. Dahl-Jensen, O. Gudmundsson, T. Bach, S. Gregersen, H. A. Pedersen, and W. Hanka. A first detailed look at the Greenland lithosphere and upper mantle, using Rayleigh wave tomography. *Geophysical Journal International*, 158(1):267–286, 2004.
41. V. Debaille, R. G. Trønnes, A. D. Brandon, T. E. Waight, D. W. Graham, and C.-T. A. Lee. Primitive off-rift basalts from Iceland and Jan Mayen: Os-isotopic evidence for a mantle source containing enriched subcontinental lithosphere. *Geochimica et Cosmochimica Acta*, 73(11):3423–3449, 2009.
42. T. H. Torsvik, H. E. F. Amundsen, R. G. Trønnes, P. V. Doubrovine, C. Gaina, N. J. Kusznir, B. Steinberger, F. Corfu, L. D. Ashwal, W. L. Griffin, S. C. Werner, and B. Jamtveit. Continental crust beneath southeast Iceland. *Proceedings of the National Academy of Sciences*, 112(15):E1818, 2015.
43. B. B. Hanan and J. G. Schilling. The dynamic evolution of the Iceland mantle plume: the lead isotope perspective. *Earth and Planetary Science Letters*, 151(1):43–60, 1997.
44. R. Wieczorek, M. S. Fantle, L. R. Kump, and G. Ravizza. Geochemical evidence for volcanic activity prior to and enhanced terrestrial weathering during the Paleocene Eocene Thermal Maximum. *Geochimica et Cosmochimica Acta*, 119:391–410, 2013.

Methods

Calculating seafloor production rates

Seafloor production (*SP*) rates (Fig. 1d), which were utilised in our volcanic CO_2 flux calculations (see page 10), were calculated using the plate model of Müller et al. (2016)[45]. We used the open source python library, *pyGPlates* (https://www.gplates.org/docs/pygplates/) in order to filter and extract the data from the plate model. For the target time-steps (t, in Myr), we broke the complete mid-ocean ridge system into a series of spreading and transform segments in order to isolate the spreading segments (j) where new oceanic crust is formed. This approach has recently become common in analysing tectonic scenarios in ocean basins[46,47,48,49]. At each segment, for each time-step, we extracted the full spreading rate (u, in km Myr^{-1}) and the length of the spreading segment (L, in km). The full spreading rate was calculated by summing the half spreading rate of each individual flank of each ridge segment, thereby sidestepping any issues pertaining to asymmetric spreading. We did this because, for the purposes of our analysis, we were only interested in the total amount of new seafloor generated. We then took the product of the spreading segment length and full spreading rate to calculate the seafloor production rate (in km^2 Myr^{-1}), and then summed the area of all segments per time-step, to obtain a total seafloor production per Myr (equation 1), as follows:

$$SP(t) = \sum_{j} uL \qquad (1)$$

Geochemical analysis of the volcanic tuffs

We carried out major, trace and isotopic analysis (variously) on 20 tuff layers sampled from DSDP Site 555 on the Rockall Plateau. X-ray fluorescence (XRF) analyses were carried out in the Grant Institute of Earth Science at the University of Edinburgh, using procedures described in refs.[50,51]. Major-element concentrations (Supplementary Table 1) were determined after fusion with a lithium borate flux containing La_2O_3 as a heavy absorber, using an existing method[52]. Rock powder was dried at 110°C for at least 1 hour, and a precisely-weighed 1-g aliquot ignited at 1100°C to determine loss on ignition (LOI). The residue was then mixed with Johnson Matthey Spectroflux 105 in a sample:flux ratio of 1:5, based on the unignited sample mass, and fused in a muffle furnace in a Pt5%Au crucible. After the initial fusion, the crucible was reweighed and any flux weight loss was made up with extra flux. After a second fusion over a Meker burner, the molten mixture was swirled several times to ensure homogeneity, cast onto a graphite mold, and flattened with an aluminium plunger into a thin disk. The mold and plunger were maintained at a temperature of 220°C on a hotplate.

Trace-element concentrations (Supplementary Table 1) were determined on pressed-powder samples. Eight grams of rock powder were mixed thoroughly with eight drops of a 2% aqueous solution of polyvinyl alcohol. The mixture was loaded into a 40-mm diameter aluminium cup in a stainless steel die and compressed against a polished tungsten carbide disc in a hydraulic press at 0.6 tons cm^{-2}. The fused and pressed samples were analysed using a PANalytical PW 2404 automatic X-ray fluorescence spectrometer with a Rh-anode X-ray tube. Trace-element background positions were placed as close as possible to peaks, and long count times were used at both peak and background positions. Where background count rates were measured on either side of the peak, as in most trace-element determinations, the count time was divided between the two positions. Analytical conditions are given in refs.[50,51].

Corrections for matrix effects on the intensities of major-element lines were made using theoretical alpha coefficients calculated on-line using the PANalytical software. The coefficients were calculated to allow for the amount of extra flux replacing volatile components in the sample so that analytical totals should be 100% less than the measured LOI. Intensities of the longer wavelength trace-element lines (La, Ce, Nd, Cu, Ni, Co, Cr, V, Ba, and Sc) were corrected for matrix effects using alpha coefficients based on major-element concentrations measured at the same time on the powder samples. Matrix corrections were applied to the intensities of the other trace-element lines by using the count rate from the RhK_α Compton scatter line as an internal standard[53]. Line-overlap corrections were applied using synthetic standards.

The spectrometer was calibrated against USGS and CRPG geochemical reference standards using the values given by Govindaraju (1994)[54], except that the values of Jochum et al. (1990)[55] were used for Nb and Zr in BCR-1 and BHVO-1. Excellent calibration lines were obtained using these standards. Analytical precision and accuracy are comparable to the values reported in refs.[50,51]. Four USGS geostandards were analysed along with the samples and the data from these (Supplementary Table 2) were used to assess accuracy and precision.

Trace element analysis was performed on a representative selection of four of the tuffs using an Inductively Coupled Plasma Mass Spectrometer (ICP-MS). Samples were homogenised using a unidirectional crushing machine prior to dissolution via a three-stage, mixed acid (HF-HNO_3-HCl) closed-vessel approach. After digestion, samples were dried down prior to resuspension in 2% HNO_3 for analysis, carried out using a Thermo Scientific X-Series-2 at the University of Southampton. Alongside samples, blanks and International standard JA-2 (ref.[56]) and Southampton internal basalt standard BRR-1 (ref.[57]) were prepared and analysed (Supplementary Table 4). Recoveries of JA-2 and BRR-1 are shown in Supplementary Table 5.

Finally, we analysed the $^{143}Nd/^{144}Nd$ isotope composition of several samples of tuff from Site 555 (Fig. 2a; Supplementary Table 3). Here, ~25 mg of freeze-dried sediment was homogenised using a pestle and mortar prior to leaching in 6M HCl for 2 hours to remove any diagenetic, alteration-related material. Samples were then digested via a mixed acid, closed vessel HNO_3-HF approach on a hotplate at 120°C. Digests were then taken to incipient dryness prior to resuspension in 2% HNO_3 for analysis. All acids were sub-boiled to ensure purity and prepared at the University of Southampton. Aliquots were then purified via first cation (AG50-X8 200-400 mesh

resin) and then reverse phase (LN Spec, Eichrom Industries) chromatography to remove isobaric interferents. All measurements were made on a Thermo Fisher Neptune Multi-Collector-ICP-MS at the University of Southampton. Mass bias corrections were performed using repeat measurements of the standard JNdi-1 (ref. [58]) with a $^{143}Nd/^{144}Nd$ value of 0.512115. Nd isotope ratios are presented using epsilon notation as follows:

$$\epsilon Nd = \left(\frac{^{143}Nd/^{144}Nd_{sample}}{^{143}Nd/^{144}Nd_{CHUR}} - 1 \right) \times 10^4 \quad (2)$$

where $^{143}Nd/^{144}Nd_{CHUR}$ is the Nd isotopic composition of the chondrite uniform reservoir, with a value of 0.512638 (ref. [59]). Precision of $^{143}Nd/^{144}Nd$ (2 SE) was between 0.000005 and 0.00001, corresponding to ϵNd precision of between 0.1 and 0.2.

Establishing a chronostratigraphic framework

We established a chronostratigraphic framework for Site 555 on the Rockall Plateau, building on a number of existing constraints at this site (Fig. 1a). The PETM as geochemically defined could not be idenitfied at this site, because of the high proportion of volcanic and siliciclastic material (Fig. 2a), intruded at many levels by dolerite dykes and sills with emplacement temperatures likely in the range ~1000° to 1250°. Thus, the adjacent sediments likely experienced temperatures >650°, thermal conditions which are known to seriously affect $\delta^{13}C$ composition in mudrocks and carbonates [60]. Accordingly, we rely on a combination of radiometric, magnetostratigraphic and paleontological age constraints, in addition to well-defined sediment accumulation rate estimates. The most reliable radiometric date in this sequence, from an olivine phyric basalt near the Palaeocene-Eocene boundary, yielded a K-Ar age of 54.5 ± 2 Ma (ref. [61]). Although uncertain, this can be narrowed further by considering the distribution of calcareous nannoplankton, including *Fasciculithus*, which disappears in the mudstones below the hyaloclastites (top NP9), with its last occurrence dated to ~55.6 Ma (http://www.mikrotax.org). This suggests that the age of the lava is most likely in the range 56.5–55.6 Ma, supporting the original position of the Palaeocene-Eocene boundary [62]. Further, the overlying mudstones interbedded with the tuffs contain the dinoflagellate cyst species, *Apectodinium augustum*[27], characteristic of the TP5a palynozone [63]. Therefore, most of the tuff layers at Site 555 (Fig. 2) were emplaced immediately prior to, and during the PETM. We estimate the duration of this eruptive phase by calculating the thickness of strata between the bottom and upper tuffs in the phase (i.e., 691 and 605.5 mbsl, respectively), and using the sediment accumulation rates (50 cm kyr^{-1}) at these levels at Site 555[4]. This gives a duration of 171 kyr, which is near-identical to that of the contemporaneous PETM interval[11,15]. However, given that the earliest tuffs occur just below the Palaeocene-Eocene boundary, the true duration is more likely to be of the order of 213 kyr, assuming that the PETM section represents the 170 kyr interval[11,15]. This interpretation is consistent with the occurrence of tuffs in the upper part of the sequence (Supplementary Fig. 2) that are geochemically similar to those reported in the PETM recovery phase elsewhere in the NAIP[4]. We therefore consider a duration range of 171–213 kyr to be most reasonable for this eruptive phase. Given the above observations, we estimate the age of basal strata in this hole (~950 m) at 56.6 Ma, which is consistent with biostratigraphy and magnetostratigraphy[4].

The base of the Milne Land Formation (Lower), which is correlated with the base of the Faeroes Middle Lava Formation[1,22] has been well-dated at 56.1 ± 0.4 Ma. Storey et al. (2007)[1] use the relative age of the well-dated Danish Ash-17 to firmly place the PETM interval after the onset of MLF volcanism. A late Palaeocene age is also supported by palynologic studies of the underlying (non-marine) coal-bearing Prestfjall Formation, and its position near the boundary between magnetic polarity chrons c24r and c25n [64] (i.e., 57.1 Ma; ref. [65]). For the Upper Lava Formation (ULF), we assumed an upper age of 55.5 Ma; this is based on an average of three radiometric ages, including one obtained from the upper ULF in the Faeroes (55.1 ± 0.5 Ma; ref. [1]). We used two radiometric ages obtained from the Skaergaard intrusion (55.75 ± 0.3 Ma, and 55.65 ± 0.3 Ma; ref. [66]), where the parental magma has been genetically linked to the Milne Land Formation [67], and accordingly its crystallisation is considered to provide an upper age constraint for Milne Land Formation volcanism[1] (and thus, the lower Geikie Plateau Formation[22]). Using this age model, we calculate the duration of the lowermost high Mg# part of the MLF (i.e., the lowermost 800 m; Fig. 2b) to be 227 kyr, similar to that of the volcanic phase at Rockall.

Establishing a chronostratigraphic framework for the Faroese Lower Lava Formation (correlative with the Nansen Fjord Formation of east Greenland) is more challenging because of the large uncertainties associated with radiometric ages through this succession[3]. However, this inherent uncertainty does not impact our results in any way; data for the lower formations are shown only for reference purposes on our stratigraphic section (Fig. 2b–c). As a reasonable solution, we used magnetic polarity chrons for the Faroes sequence [68], combined with the chemical stratigraphy of Larsen et al. (1999)[22] and using a standard geomagnetic polarity time scale [65]. We calibrated the ages at certain depths in the succession using the ages of chron boundaries as tie points, and applying a linear interpolation between these known points (which assumes constant lava accumulation rates). We found that this age model was broadly consistent with existing radiometric ages (i.e., in most cases within uncertainty)[3].

REE melting model

A simple batch melting equation was used in the construction of Figure 2e:

$$C_L/C_0 = \frac{1}{D + F - PF} \quad (3)$$

where C_0 is the initial concentration of some element in the mantle source, C_L is its concentrations in the liquid, F is the melt fraction, D is the average distribution coefficient for the mantle phases weighted by their respective mass fractions

before the onset of melting, and P is the average distribution coefficient for the mantle phases weighted by their respective contribution to the melt. We use a peridotite mantle source with a mineralogical composition given by McKenzie and O'Nions (1991)[69]: (1) 57.8% olivine, 27.0% orthopyroxene, 11.9% clinopyroxene and 3.3% spinel (spinel lherzolite); and (2) 59.8% olivine, 21.1% orthopyroxene, 7.6% clinopyroxene and 11.5% garnet (garnet lherzolite). Partition coefficients (D) vary significantly with pressure, temperature and liquid composition, and this limits the reliability of partial melting models since the choice of values is always somewhat subjective. Here we have attempted to be more objective by using averages of all appropriate published D values (Supplementary Table 6). We use the following mantle melting proportions for spinel lherzolite (equation 4; ref. [70]) and garnet lherzolite (equation 5; ref. [71]):

$$liquid = -0.22\,ol + 0.38\,opx + 0.71\,cpx + 0.13\,sp \quad (4)$$

$$liquid = 0.08\,ol - 0.19\,opx + 0.81\,cpx + 0.30\,gt \quad (5)$$

where ol is olivine, opx is orthopyroxene, sp is spinel, cpx is clinopyroxene and gt is garnet.

The concentrations of REE in our mantle source (Ce 1.236 ppm, Sm 0.346 ppm, Yb 0.432 ppm) are calculated from the composition of primitive basalt from the Ontong Java Plateau and are thought to be typical of mantle plumes[72].

Please note that Supplementary Table 6 cites additional references[73,74,75,76,77,78,79,80].

Modelling of CO_2 fluxes

We perform a simple Monte Carlo simulation, sampling from probability distributions for six uncertain parameters (Supplementary Tables 7–8) to estimate the probable combined CO_2 emissions from incipient ridge volcanism and active large igneous provinces (LIPs). This enables us to evaluate the relative contributions to carbon release during the PETM due to ridge production and LIP formation. We also calculate the effect of incorporating carbonated SCLM melt in different amounts during enhanced melting along the ridge axis. In our calculations, we assumed a PETM duration of 170 kyr (ref.[15]), which is supported by recent astrochronological solutions[11].

We use Beta distributions to represent uncertainty in the parameters (Supplementary Table 8). The Beta distribution is a continuous distribution over a fixed interval [0, 1], but can be rescaled to any desired range. It is defined by two shape parameters α and β, which can be estimated from the distribution mean (μ) and variance (σ^2):

$$\alpha = \mu\left(\mu\,\frac{(1-\mu)}{\sigma^2} - 1\right) \quad (6)$$

$$\beta = \alpha\left(\frac{1}{\mu} - 1\right) \quad (7)$$

where μ = the mean, σ = standard deviation, and σ^2 = the variance. To estimate Beta distribution parameters, we use best estimates (from published data and observations) of the minimum, mean and maximum values for each variable (Supplementary Table 8, and discussed below), and apply these to equations 6 and 7 above (using re-scaled values for μ and σ). For simplicity we assume that the standard deviation for a given variable is 20% of the range, σ_v = 0.2 (max–min). The inputs to the calculations (sampled, constant and fixed) and outputs are listed in Supplementary Tables 7–8 and the corresponding histograms for each of the sampled variables are shown in Supplementary Fig. 3.

To quantify the CO_2 degassing flux from ridges in the NAIP (i.e., the North Atlantic and the Labrador Sea), we used seafloor production rates parameterised from plate-tectonic reconstructions (see above) for the ridges at 55 Ma—the first time step at which seafloor generation is recorded in the North Atlantic. In these calculations we assumed an oceanic crustal thickness of 6 km, the global average[81]. Only a small fraction of the total amount of CO_2 available in the basaltic oceanic crust is degassed at ridges. To estimate this, we used the ratio between the oceanic crustal productivity (i.e., the total amount of crust formed, which is ~18 km^3 yr^{-1}) and the estimated CO_2 fluxes from the present-day global ridge system (7×10^{11} mol yr^{-1}; a middle value of ref.[20]). This analysis indicates that about 10% of the CO_2 available in the ocean crust is degassed at ridges (see main text), corresponding to the upper 600 m. Thus, in our simulations we used a Beta distribution with a mean value of 10% (i.e., 10% of the total available CO_2 is lost from the crust), and minimum and maximum values of 5% and 15%, respectively. For the pre-eruptive CO_2 content of basaltic magmas, we used a Beta distribution with a mean value of 0.5 wt%, and minimum and maximum values of 0.2 wt% and 2 wt%, considered reasonable for flood basalts[19] and ocean crust at this time[82].

To estimate the CO_2 fluxes from LIPs, we used existing eruptive rate estimates for the NAIP[9]. We consider two LIP eruptive rate scenarios: (S1) low flood basalt productivity (0.6 km^3 yr^{-1}); and (S2) high productivity (2.4 km^3 yr^{-1}; ref.[9]). The combined fluxes from incipient ridge volcanism and each of these eruptive scenarios for LIPs are shown as the grey lines on our cumulative distribution functions (Fig. 3). We assumed near-total loss of CO_2 from flood basalt volcanism (mean 95%, minimum 90%, maximum 100% loss), based on observations from fresh basaltic glass in flood basalts that show most of the CO_2 is lost to degassing[19]. Ridge and LIP CO_2 outgassing was calculated using equation 8:

$$W_{COcean} = \frac{12}{44}\frac{t_{rift}}{10^{12}}(O_{Floss}.r_{basaltprod}.\rho_{basalt}.B_{FractCO2}) + (C_{FractLIP}.r_{LIPprod}.\rho_{basalt}.B_{FractCO2}) \quad (8)$$

where W_{COcean} = total weight of C released from the ocean crust and LIPs; t_{rift} is the duration of extension in years; O_{Floss} = fraction of CO_2 lost from the ocean crust; $r_{basaltprod}$ = volumetric rate of basalt production from the NAIP ridges (see equation 1); ρ_{basalt} = density of basalt (3000 kg m^{-3}); $B_{FractCO2}$ = CO_2 content (weight percent) of basalt, expressed as a fraction;

$C_{FractLIP}$ = fraction of LIPs that is fully degassed of CO_2; and $r_{LIPprod}$ = volumetric rate of basalt production from LIPs. Note that a factor of 12/44 converts from mass of CO_2 to mass of C.

The combined carbon flux estimates show that outgassing from ridges and LIPs alone are insufficient to trigger PETM warming, unless they are augmented by a transient increase in CO_2 content (as we propose, via the incorporation of carbonated SCLM during mantle melting). To account for this apparent deficit, we estimated the potential influence of SCLM melting contributions, using scenarios S1 and S2 (above) as a baseline (i.e., the background volcanic carbon flux; Fig. 3). During continental extension (as in the early Cenozoic North Atlantic) the deep metasomatized mantle lithosphere is stretched, exhumed, and melted along the length of the newly-formed ridge[39]. We estimated the total volume of carbonated SCLM (c-SCLM) from the length of the ridge segments active between 56–55 Ma (Fig. 1d), assuming a plausible range of thicknesses and melting widths for this layer (Supplementary Table 8).

The precise thickness of the c-SCLM of the North Atlantic craton at 55 Ma is poorly constrained and is likely to have been spatially heterogeneous, but is considered to lie in the range 10 km (ref.[39]) to ~30 km thick (based on chemical tomography of cratonic regions[83]). This is broadly consistent with geochemical and tectono-magmatic models of the North Atlantic craton[84,85]. We assume a mean c-SCLM thickness of 20 km, with minimum and maximum values of 5 and 25 km. We estimated the width of SCLM involved in melting, using petrological-thermomechanical models of lithospheric rifting processes[39]. In cases where the lithosphere is about 200 km thick, the width of the melting zone is most likely to be of the order of 25 km (ref.[39]). We therefore used a Beta distribution with a mean width of 25 km and range of 5 to 30 km. SCLM melting occurs on both sides of the stretching lithosphere, doubling the total contribution to CO_2 output. c-SCLM is expected to have a high CO_2 content, of the order 5–8 wt%, but potentially even higher[37]. We therefore use a mean value of 5 wt%, minimum of 1 wt% and maximum of 10 wt%. The total contribution of SCLM melting to fluxes was estimated using equation 9:

$$W_{CSCLM} = \frac{l_{SCLM}.w_{SCLM}.h_{SCLM}.\rho_{SCLM}}{10^{12}} \quad (9)$$

where W_{CSCLM} = total weight of carbon in the SCLM (Gt); l_{SCLM} = length of SCLM involved in melting along the North Atlantic mid-ocean ridge system; w_{SCLM} = width of the SCLM zone (km); h_{SCLM} = thickness of the SCLM (km), and ρ_{SCLM} = density of SCLM (lherzolite; 3200 kg m^{-3}). A factor of $1/10^{12}$ converts weight from kg to Gt. Finally, we calculated the total weight of carbon (W_{TotalC}) produced from the ocean crust, LIPs and enhanced melting of the c-SCLM using equation 10:

$$W_{TotalC} = W_{COcean} + F_{CSCLM} W_{CSCLM} \quad (10)$$

where F_{CSCLM} is the fraction of c-SCLM melted during extension (calculated with 0.04, 0.05 and 0.08; see Fig. 3).

Please note that additional references are cited in the Supplementary Figures and Tables[86,87,88,89,90,91].

Data availability

All data generated or analysed during this study are provided in the online version of this article and in Supplementary Tables 1–8.

Code availability

The numerical modelling codes associated with this paper are available from the corresponding author (Thomas.Gernon@noc.soton.ac.uk) upon reasonable request. The map in Fig. 1a was plotted with open software GMT (under a GNU Lesser General Public License), and the map in Fig. 1b was plotted with open software GPlates (licensed for distribution under a GNU General Public License).

References

45. R. D. Müller, M. Seton, S. Zahirovic, S. E. Williams, K. J. Matthews, N. M. Wright, G. E. Shephard, K. T. Maloney, N. Barnett-Moore, M. Hosseinpour, D. J. Bower, and J. Cannon. Ocean basin evolution and global-scale plate reorganization events since Pangea breakup. *Annual Review of Earth and Planetary Sciences*, 44(1):107–138, 2016.
46. K. S. Karlsen, C. P. Conrad, and V. Magni. Deep water cycling and sea level change since the breakup of Pangea. *Geochemistry, Geophysics, Geosystems*, 20(6):2919–2935, 2019.
47. K. S. Karlsen, M. Domeier, C. Gaina, and C. P. Conrad. A tracer-based algorithm for automatic generation of seafloor age grids from plate tectonic reconstructions. *Computers & Geosciences*, 140:104508, 2020.
48. A. S. Merdith, S. E. Atkins, and M. G. Tetley. Tectonic controls on carbon and serpentinite storage in subducted upper oceanic lithosphere for the past 320 Ma. *Frontiers in Earth Science*, 7:332, 2019.
49. A. S. Merdith, P. G. del Real, I. Daniel, M. Andreani, N. M. Wright, and N. Coltice. Pulsated global hydrogen and methane flux at mid-ocean ridges driven by Pangea breakup. *Geochemistry, Geophysics, Geosystems*, 21(4):e2019GC008869, 2020.
50. J. Fitton, A. Saunders, L. Larsen, B. Hardarson, and M. Norry. Volcanic rocks from the southeast Greenland Margin at 63 °N: composition, petrogenesis, and mantle sources. *Proceedings of the Ocean Drilling Program: Scientific Results*, 152:331–350, 1998.
51. J. G. Fitton and M. Godard. Origin and evolution of magmas on the Ontong Java Plateau. *Geological Society, London, Special Publications*, 229(1):151–178, 2004.
52. K Norrish and J. T Hutton. An accurate X-ray spectrographic method for the analysis of a wide range of geological samples. *Geochimica et Cosmochimica Acta*, 33(4):431–453, 1969.
53. R. C. Reynolds. Matrix corrections in trace element analysis by X-ray fluorescence: Estimation of the mass absorption coefficient by Compton scattering. *American Mineralogist*, 48(9-10):1133–1143, 1963.
54. K. Govindaraju. 1994 compilation of working values and sample description for 383 geostandards. *Geostandards Newsletter*, 18(S1):1–158, 1994.
55. K. P. Jochum, H. M. Seufert, and M. F. Thirlwall. High-sensitivity Nb analysis by spark-source mass spectrometry (SSMS) and calibration of XRF Nb and Zr. *Chemical Geology*, 81(1):1–16, 1990.
56. N. Imai, S. Terashima, S. Itoh, and A. Ando. 1994 compilation of analytical data for minor and trace elements in seventeen GSJ geochemical reference samples, "igneous rock series". *Geostandards Newsletter*, 19(2):135–213, 1995.
57. B. J. Murton, R. N. Taylor, and M. F. Thirlwall. Plume–ridge interaction: a geochemical perspective from the Reykjanes Ridge. *Journal of Petrology*, 43(11):1987–2012, 2002.

58. T. Tanaka, S. Togashi, H. Kamioka, H. Amakawa, H. Kagami, T. Hamamoto, M. Yuhara, Y. Orihashi, S. Yoneda, H. Shimizu, T. Kunimaru, K. Takahashi, T. Yanagi, T. Nakano, H. Fujimaki, R. Shinjo, Y. Asahara, M. Tanimizu, and C. Dragusanu. JNdi-1: a neodymium isotopic reference in consistency with LaJolla neodymium. *Chemical Geology*, 168(3):279–281, 2000.
59. S. B. Jacobsen and G. J. Wasserburg. Sm-Nd isotopic evolution of chondrites. *Earth and Planetary Science Letters*, 50(1):139–155, 1980.
60. L. E. Munro, F. J. Longstaffe, and C. D. White. Effects of heating on the carbon and oxygen-isotope compositions of structural carbonate in bioapatite from modern deer bone. *Palaeogeography, Palaeoclimatology, Palaeoecology*, 266(3):142–150, 2008.
61. R. M. Macintyre and P.J. Hamilton. Isotopic geochemistry of lavas at DSDP Holes 81-553 and 81-555. In *DSDP Initial Reports*, chapter 30, pages 775–781. 1984.
62. D. G. Roberts, J. Backman, A. C. Morton, J. W. Murray, and J. B. Keene. Evolution of volcanic rifted margins: Synthesis of Leg 81 results on the west margin of Rockall Plateau. In *DSDP Initial Reports*, chapter 39, pages 883–911. 1984.
63. W. A. Berggren, D. V. Kent, C. C. Swisher, and M. P. Aubrey. A revised Cenozoic geochronology and chronostratigraphy. *Society for Sedimentary Geology Special Publication*, 54:129–212, 1995.
64. J. Lund. A late Paleocene non-marine microflora from the interbasaltic coals of the Faeroe Islands, North Atlantic. *Bulletin of the Geological Society of Denmark*, 37:181–203, 1988.
65. J. G. Ogg. *Chapter 5 - Geomagnetic Polarity Time Scale*, chapter 5, pages 85–113. Elsevier, Boston, 2012.
66. M. M. Hirschmann, P. R. Renne, and A. R. McBirney. $^{40}Ar/^{39}Ar$ dating of the Skaergaard intrusion. *Earth and Planetary Science Letters*, 146(3):645–658, 1997.
67. J. K. Jakobsen, C. Tegner, C. K. Brooks, A. J. R. Kent, C. E. Lesher, T. F. D. Nielsen, and M. Wiedenbeck. Parental magma of the Skaergaard intrusion: constraints from melt inclusions in primitive troctolite blocks and FG-1 dykes. *Contributions to Mineralogy and Petrology*, 159(1):61–79, 2009.
68. R. Waagstein. Structure, composition and age of the Faeroe basalt plateau. *Geological Society, London, Special Publications*, 39(1):225–238, 1988.
69. D. McKenzie and R. K. O'Nions. Partial melt distributions from inversion of rare earth element concentrations. *Journal of Petrology*, 32(5):1021–1091, 7/16/2020 1991.
70. M. B. Baker and E. M. Stolper. Determining the composition of high-pressure mantle melts using diamond aggregates. *Geochimica et Cosmochimica Acta*, 58(13):2811–2827, 1994.
71. M. J. Walter. Melting of garnet peridotite and the origin of komatiite and depleted lithosphere. *Journal of Petrology*, 39(1):29–60, 1998.
72. A. R. Hastie, J. G. Fitton, A. C. Kerr, I. McDonald, A. Schwindrofska, and K. Hoernle. The composition of mantle plumes and the deep earth. *Earth and Planetary Science Letters*, 444:13–25, 2016.
73. S. R. Hart and T. Dunn. Experimental cpx/melt partitioning of 24 trace elements. *Contributions to Mineralogy and Petrology*, 113(1):1–8, 1993.
74. E. H. Hauri, T. P. Wagner, and T. L. Grove. Experimental and natural partitioning of Th, U, Pb and other trace elements between garnet, clinopyroxene and basaltic melts. *Chemical Geology*, 117(1):149–166, 1994.
75. K. T. M. Johnson. Experimental determination of partition coefficients for rare earth and high-field-strength elements between clinopyroxene, garnet, and basaltic melt at high pressures. *Contributions to Mineralogy and Petrology*, 133(1):60–68, 1998.
76. P. McDade, J. D. Blundy, and B. J. Wood. Trace element partitioning on the Tinaquillo Lherzolite solidus at 1.5GPa. *Physics of the Earth and Planetary Interiors*, 139(1):129–147, 2003.
77. V. J. M. Salters, J. E. Longhi, and M. Bizimis. Near mantle solidus trace element partitioning at pressures up to 3.4 GPa. *Geochemistry, Geophysics, Geosystems*, 3(7):1–23, 2002.
78. T. Skulski, W. Minarik, and E. B. Watson. High-pressure experimental trace-element partitioning between clinopyroxene and basaltic melts. *Chemical Geology*, 117(1):127–147, 1994.
79. J. Tuff and S. A. Gibson. Trace-element partitioning between garnet, clinopyroxene and Fe-rich picritic melts at 3 to 7 GPa. *Contributions to Mineralogy and Petrology*, 153(4):369–387, 2007.
80. A. J. Irving. A review of experimental studies of crystal/liquid trace element partitioning. *Geochimica et Cosmochimica Acta*, 42(6):743–770, 1978.
81. M. R. Perfit and J. H. Steele. *Mid-Ocean Ridge Geochemistry and Petrology*, pages 815–825. Academic Press, Oxford, 2001.
82. R. D. Müller and A. Dutkiewicz. Oceanic crustal carbon cycle drives 26-million-year atmospheric carbon dioxide periodicities. *Science Advances*, 4(2):eaaq0500, 2018.
83. S. Y. O'Reilly and W. L. Griffin. Imaging global chemical and thermal heterogeneity in the subcontinental lithospheric mantle with garnets and xenoliths: Geophysical implications. *Tectonophysics*, 416(1):289–309, 2006.
84. S. Tappe, S. F. Foley, A. Stracke, R. L. Romer, B. A. Kjarsgaard, L. M. Heaman, and N. Joyce. Craton reactivation on the Labrador Sea margins: $^{40}Ar/^{39}Ar$ age and Sr–Nd–Hf–Pb isotope constraints from alkaline and carbonatite intrusives. *Earth and Planetary Science Letters*, 256(3):433–454, 2007.
85. S. Tappe, R. L. Romer, A. Stracke, A. Steenfelt, K. A. Smart, K. Muehlenbachs, and T. H. Torsvik. Sources and mobility of carbonate melts beneath cratons, with implications for deep carbon cycling, metasomatism and rift initiation. *Earth and Planetary Science Letters*, 466:152–167, 2017.
86. T. M. Gernon, B. G. J. Upton, R. Ugra, C. Yücel, R. N. Taylor, and H. Elliott. Complex subvolcanic magma plumbing system of an alkali basaltic maar-diatreme volcano (Elie Ness, Fife, Scotland). *Lithos*, 264:70–85, 2016.
87. M. J. Le Bas, R. W. Le Maitre, A. Streckeisen, and B. Zanettin. A chemical classification of volcanic rocks based on the total alkali-silica diagram. *Journal of Petrology*, 27(3):745–750, 1986.
88. L.M. Chambers. *Age and duration of the British Tertiary Igneous Province: implications for the development of the ancestral Iceland plume*. PhD thesis, University of Edinburgh, 2000.
89. J. A. Brodie and J. G. Fitton. Data report: Composition of basaltic lavas from the seaward-dipping reflector sequence recovered during Deep Sea Drilling Project Leg 81 (Hatton Bank). In *Proceedings of the Ocean Drilling Program, Scientific Results*, volume 152, pages 431–435, 1998.
90. J. G. Fitton, J. J. Mahoney, P. J. Wallace, and A. D. Saunders. Origin and evolution of the Ontong Java Plateau: introduction. *Geological Society, London, Special Publications*, 229(1):1–8, 2004.
91. W. F. McDonough and S. s. Sun. The composition of the Earth. *Chemical Geology*, 120(3):223–253, 1995.

Acknowledgements

This study was supported by a Natural Environment Research Council (NERC) grant (NE/R004978/1) to T.G., which also supported T.H. T.G. and T.H. received funding from the Alan Turing Institute, the UK's national institute for data science and artificial intelligence (EP/N510129/1). J.L. was supported by NERC grant NE/K00543X/1 awarded to M.P. and T.G. T.G. acknowledges the Distinguished Geologists' Memorial Fund of the Geological Society of London to sample the Rockall tuffs at the IODP Bremen Core Repository (BCR). We are grateful to the staff of the BCR, especially W. Hale, for their assistance, and to M. Cooper, A. Michalik and A. Milton (University of Southampton) for laboratory assistance. R.N.M. was supported by a Key Research Program of the Institute of Geology & Geophysics, CAS, grant (No. IGGCAS-201905). We thank G. Hincks for illustrating the early Cenozoic North Atlantic ridge (Fig. 4).

Author contributions

T.G. conceived the idea, led the study, interpreted the data and prepared the manuscript and figures. T.H. performed the modelling, with input from T.G. R.N.M. assisted with tectonic and geodynamic interpretation, and G.F., J.L., R.B. and

M.P. provided support with geochemical analysis and interpretation. G.F. carried out the melt modelling. A.M. calculated the seafloor production rates and provided support with *GPlates* and *pyGPlates*. T.G. wrote the manuscript with input from all co-authors.

Competing interests:

The authors declare no competing interests.

Additional information

Supplementary information is available for this paper at https://doi.org/10.1038/s12345-111-2222-3.
Correspondence and requests for materials should be addressed to T.G.
Peer review information *Nature Geoscience* thanks [reviewers] for their contribution to the peer review of this work.
Reprints and permissions information is available at http://www.nature.com/reprints.

Figures

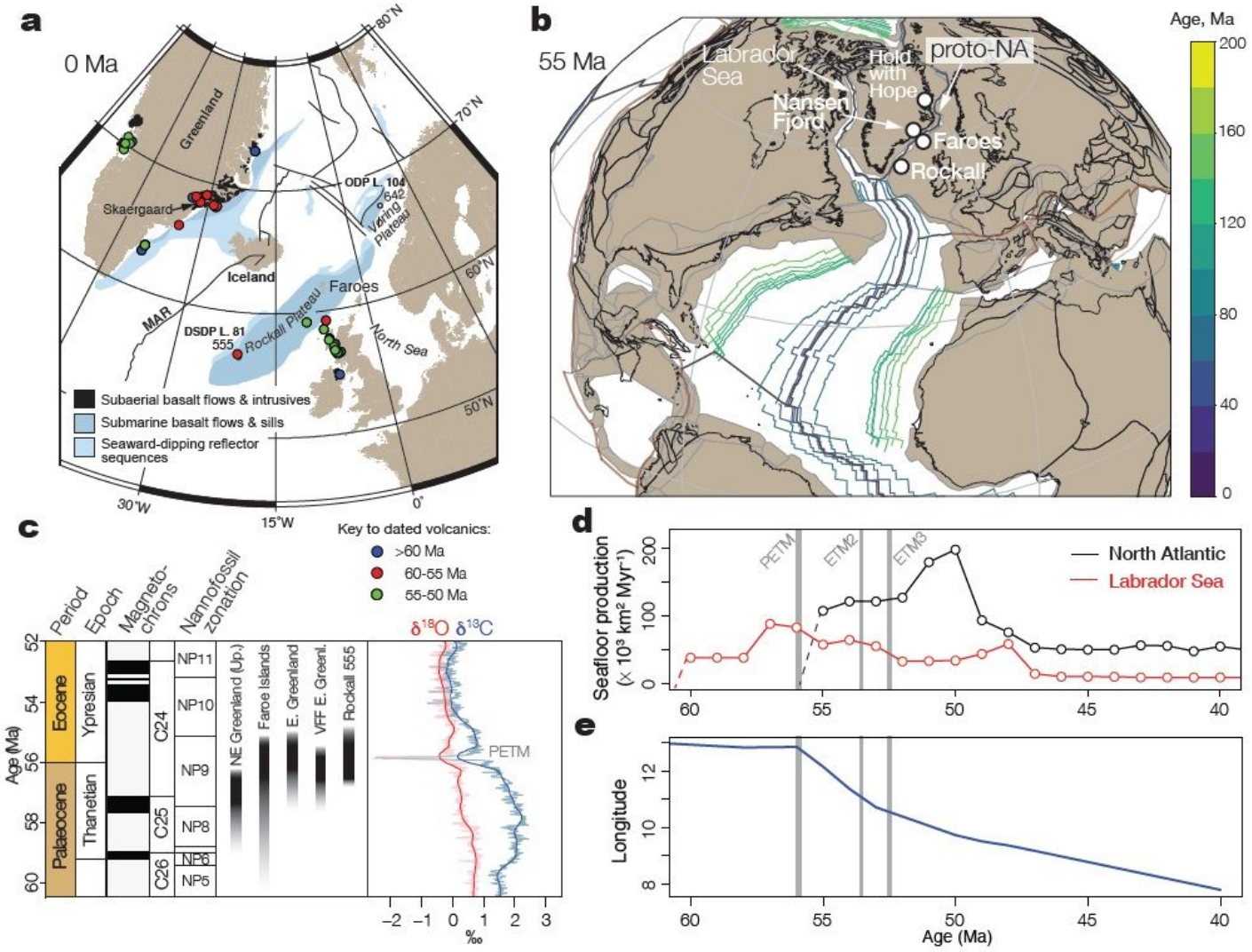

Figure 1

Early Cenozoic tectonic and magmatic evolution of the North Atlantic region j a, Map of the present-day North Atlantic region showing the distribution of Palaeocene–Eocene lava flows and intrusives 1, with dated volcanics denoted by colored symbols 2. b, Plate tectonic reconstruction showing nascent ridge systems developing along the Labrador Sea and North Atlantic. c, Ages of the volcanic sections discussed (Up=Upper; VFF=Vandfaldsdalen Fm), defined by radiometric dates 1,3, magnetostratigraphy and nannofossil zonation 4,5,6, and corresponding carbon and oxygen isotope records showing the PETM isotope excursions (solid and faint lines show 1 Myr and 20 kyr locally weighted functions, respectively) 7. d, Seafloor production rates for the Labrador Sea and North Atlantic, derived from GPlates (Methods), shown alongside the timing of Eocene hyperthermals. (E) Palaeolongitude of Greenland 8 indicating the onset of ocean crustal production in the North Atlantic and ridge push at 56 Ma.

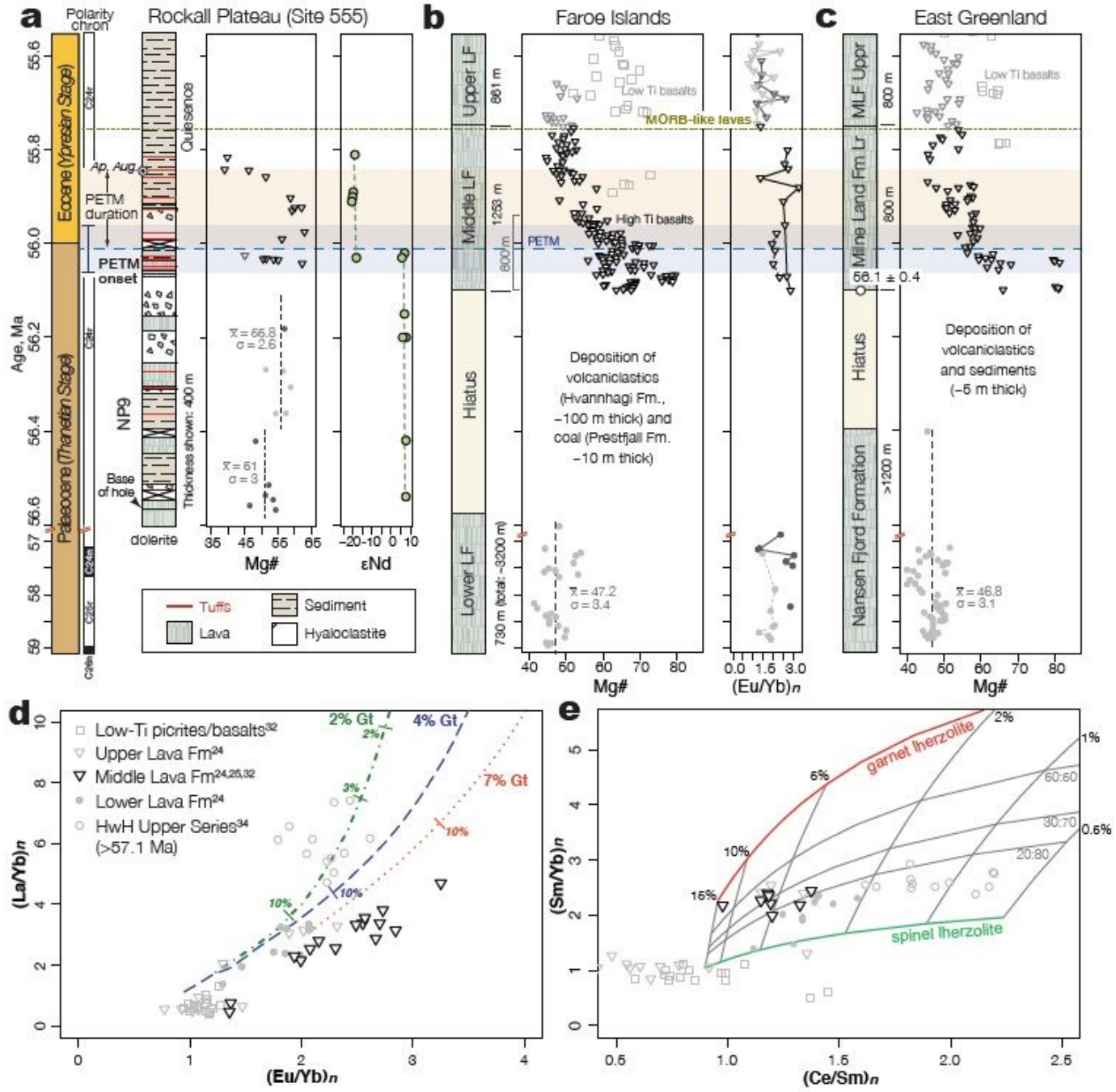

Figure 2

Palaeocene-Eocene volcanostratigraphy and geochemistry of the proto-North Atlantic ridge. a, Simplified log of the Rockall 'Phase 1' sequence 21 showing lithologies, Mg# (i.e., 100 x molecular MgO/(MgO + FeO), where FeO is assumed to be 0.9FeOT), and eNd (Supplementary Fig. 1). b, Simplified log of the Faroes Basalt Formations 22, with Mg# and (Eu/Yb)n (chondrite-normalized 23); Mg# data are from 22 and (Eu/Yb)n are from 24,25; note the sharp transition to high Mg# (and enriched REE contents) at ca. 56.1 Ma1, which is also observed in c, east Greenland (Milne Land Formation) 22. d, (La/Yb)n vs (Eu/Yb)n of the Faroes and Hold with Hope (HwH) lavas (chondrite-normalized 23) and modeled non-modal batch melting of a lherzolitic mantle source, adopted from 26, showing different degrees of

melting of a garnet lherzolite (green, blue and red curves). e, (Sm/Yb)n vs (Ce/Sm)n and an REE melting model (Methods), showing percentage melt along the top and the relative proportions of garnet- and spinel-lherzolites from 100% gt-lherzolite (red curve) to 100% sp-lherzolite (green curve). Both models indicate that the Faroes Middle Lava Formation (i.e., high Mg# basalts in the lower 500 m of the MLF; see (b), that erupted immediately prior to and during the PETM, experienced the highest degrees of melting of a mantle source containing &10% garnet.

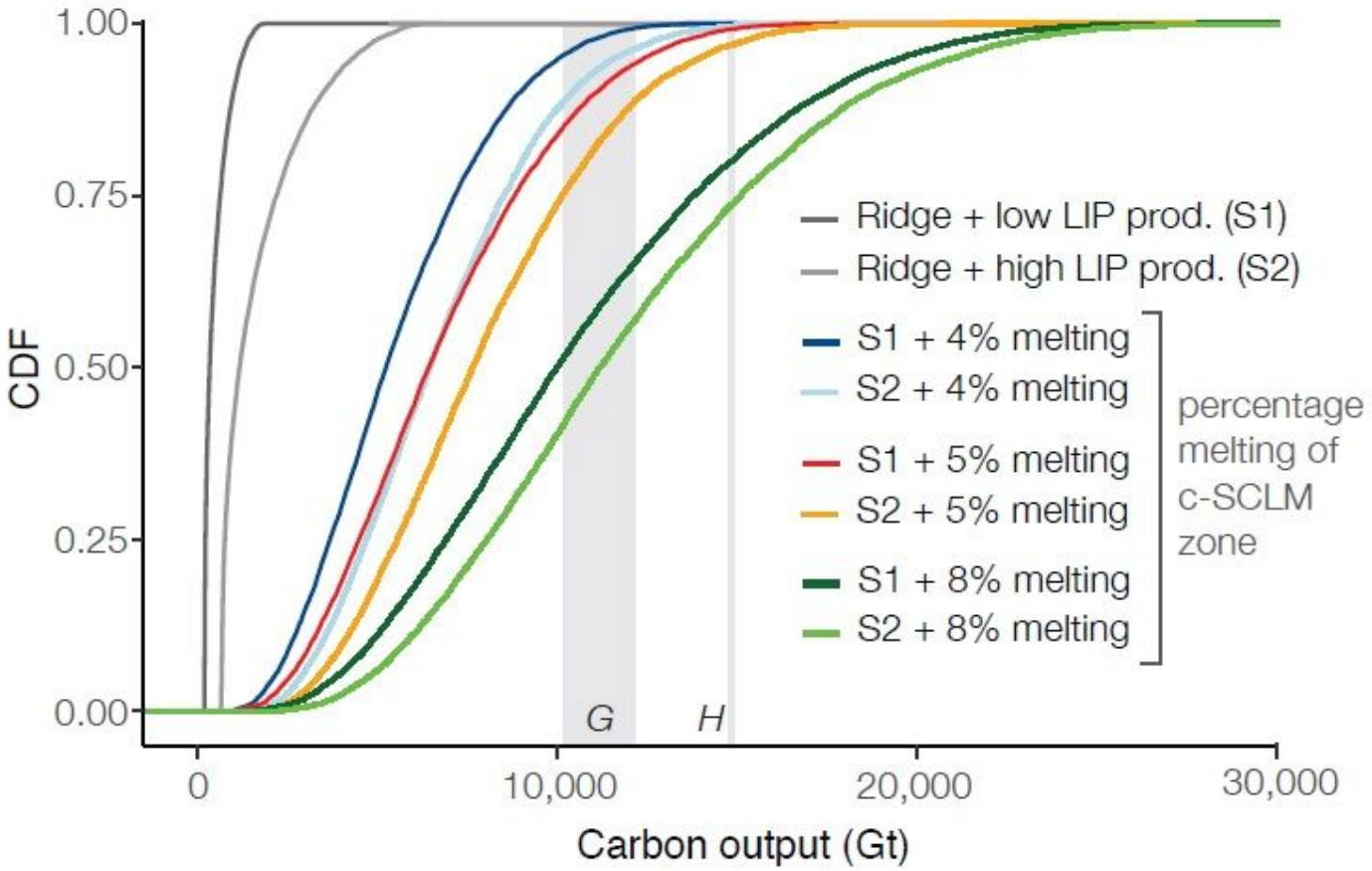

Figure 3

Simulations of volcanic carbon release during the PETM. Results are plotted as cumulative distribution functions (CDFs). The gray lines show the estimated carbon output from ridge volcanism and LIPs alone; with S1 and S2 showing low (0.6 km3 yr x 1) and high (2.4 km3 yr x1) LIP eruption rate scenarios 9, respectively (Supplementary Fig. 3) (see Methods). The coloured lines show the effects of adding 4% to 8% carbonated (c–) SCLM melt along the incipient ridge during breakup. The gray vertical bars denote the carbon output necessary to drive and sustain PETM warming estimated by Gutjahr et al. 14 (labelled G; 10,200–12,200 Gt C), and Haynes & H¨onisch 16 (labelled H; 14,900 Gt C).

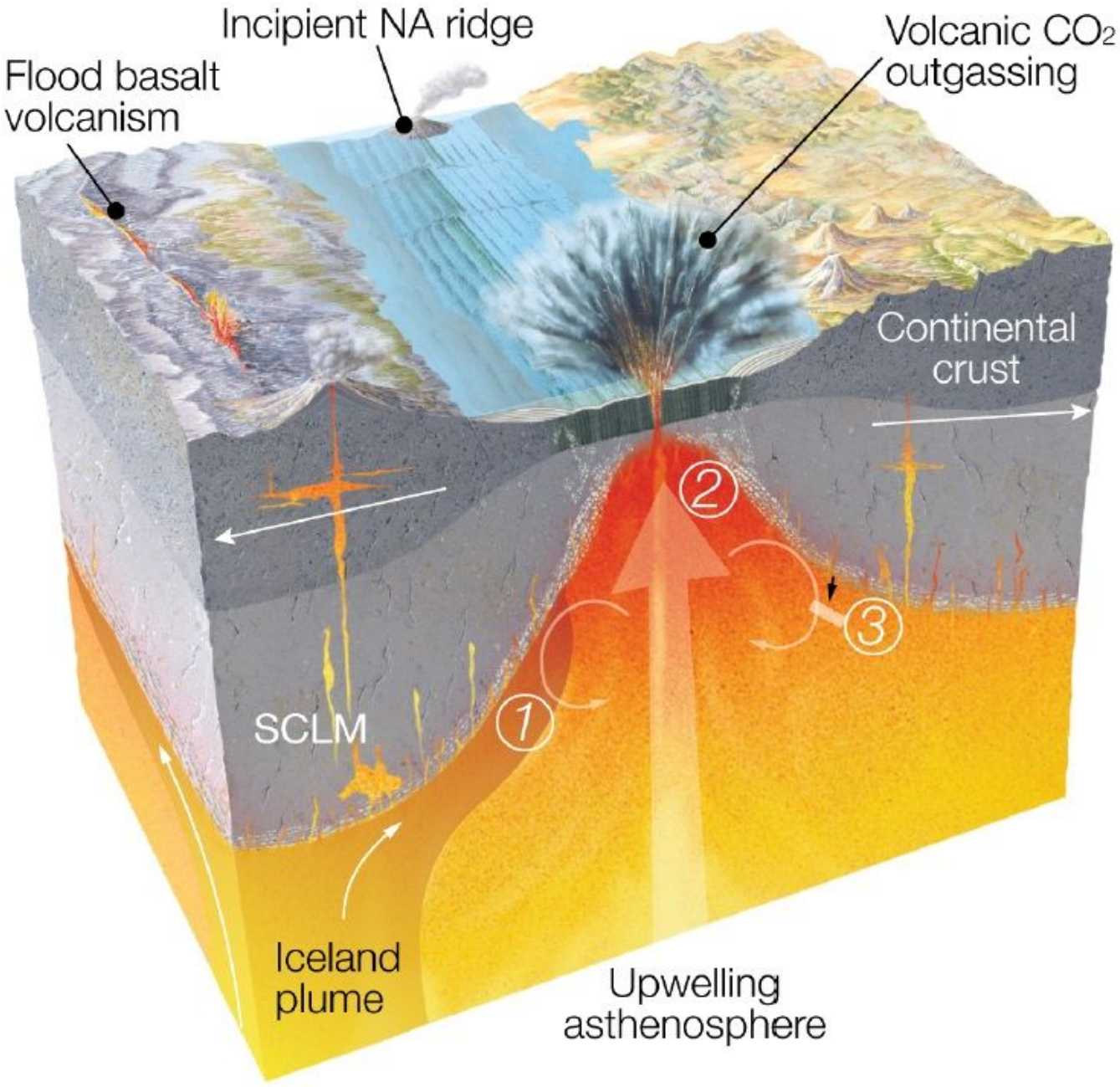

Figure 4

Volcanic carbon release in the North Atlantic during the PETM. Model stages: 1, progressive thermo-mechanical weakening of the sub-continental lithospheric mantle (SCLM) by the Iceland plume; 2, disruption of the ruptured metasomatized SCLM zone by incipient asthenospheric upwelling; 3, delamination of carbonated fragments of the deep SCLM during lithospheric stretching, which generate the enduring enriched components ('EM1') still present in the Icelandic mantle today 41.

Supplementary Files

This is a list of supplementary files associated with this preprint. Click to download.

- SupplementaryInformationNGS20210300519.pdf